Chen *et al. Journal of Nanobiotechnology* (2025) 23:393
https://doi.org/10.1186/s12951-025-03400-3

Journal of Nanobiotechnology

RESEARCH Open Access

Interplay between material properties and cellular effects drives distinct pattern of interaction of graphene oxide with cancer and non-cancer cells

Yingxian Chen[1,2], Vinicio Rosano[1,2], Neus Lozano[3,4], YuYoung Shin[5], Aleksandr Mironov[6], David Spiller[7], Cinzia Casiraghi[5], Kostas Kostarelos[2,3,8,4*] and Sandra Vranic[1,2*]

Abstract

Understanding how graphene oxide (GO) interacts with cells is crucial for its safe and efficient biomedical applications. Despite extensive research, a systematic investigation using a panel of cell lines, thoroughly characterized label-free nanomaterials, and complementary analytical techniques is lacking. Here, we examined the uptake of thin GO sheets with distinct lateral dimensions in 13 cell lines: 8 cancer (HeLa, A549, PC3, DU-145, LNCaP, SW-480, SH-SY5Y, U87-MG) and 5 non-cancer (BEAS-2B, NIH/3T3, PNT-2, HaCaT, 293T), using confocal microscopy, transmission electron microscopy, and flow cytometry. Our results reveal a striking difference in GO uptake: non-cancer cells internalized GO efficiently, while in cancer cells, GO predominantly interacted with the plasma membrane, showing minimal to no internalization. Comparison to other nanomaterials (polystyrene beads and graphene flakes) confirmed that cancer cells internalize materials similarly to non-cancer cells, indicating GO-specific interactions. We identified that GO's thinness plays important role in this differential uptake. More importantly, GO disrupts the actin cytoskeleton of cancer cells, impairing the migration in cancer but not in non-cancer cells. We propose that thin GO sheets act as a cue upon interaction with the plasma membrane of cancer cell lines, subsequently inducing actin filaments disruption leading to impaired endocytosis, migration activity, and reduced capacity of cancer cells towards GO uptake.

*Correspondence:
Kostas Kostarelos
kostas.kostarelos@manchester.ac.uk
Sandra Vranic
sandra.vranic@manchester.ac.uk
[1]Nano-Cell Biology Lab, Division of Cell Matrix Biology & Regenerative Medicine, School of Biological Sciences, Faculty of Biology, Medicine and Health, The University of Manchester, Manchester, UK
[2]Centre for Nanotechnology in Medicine, Faculty of Biology, Medicine and Health, The University of Manchester, Manchester, UK
[3]Nanomedicine Lab, Catalan Institute of Nanoscience and Nanotechnology (ICN2), CSIC and BIST, Campus UAB, Barcelona, Spain
[4]Institute of Neuroscience, Universitat Autònoma de Barcelona, Barcelona, Spain
[5]Department of Chemistry, University of Manchester, Oxford Road, Manchester, UK
[6]Electron Microscopy Core Facility (RRID: SCR_021147), FBMH, University of Manchester, Manchester, UK
[7]Faculty of Biology, Medicine and Health, FBMH Platform Sciences, Enabling Technologies & Infrastructure, FBMH Research & Innovation, The University of Manchester, Michael Smith Building, Manchester M13 9PT, UK
[8]Institució Catalana de Recerca i Estudis Avançats (ICREA), Pg. Lluís Companys 23, Barcelona, Spain

Introduction

Graphene oxide (GO), due to aqueous dispersibility, large surface area suitable for the loading of therapeutic cargos through surface functionalisation and excellent biocompatibility has received extensive research interest for various biomedical applications [1, 2, 3]. However, to fully explore the biomedical potential of GO and assure its safe use, it is crucial to understand how GO interacts with biological systems at the cellular level.

Currently, a considerable number of in vitro studies have investigated interactions and uptake profile of GO. These studies mostly focused on cancer [4, 5, 6, 7, 8, 9, 10, 11, 12, 13, 14, 15, 16, 17, 18, 19, 20, 21, 22, 23, 24, 25, 26, normal27, 28, 29, 30, 31, 32, or immune cells33, 34, 35], with the vast majority of the studies using immortalised, commercially available cell lines. Considering the surging interest in using GO in cancer therapy, especially as drug carriers, it is critical to understand the uptake pattern of GO in cancer and normal cells. Some studies have compared the uptake of GO between cancer and normal cells [36, 37, 38, 39, cancer and immune cells40, 41, 42, 43], or a combination of cancer, normal, and immune cells [44, 45, 46]. However, these studies largely used only one of each cell type [36, 40, 41, 44] or a total of no more than three cell lines for comparison [38, 39, 42, 43, 46]. One study examined the uptake of GO in six cell lines (three cancer, one normal, and two immune cell lines) and reported uptake of GO only in immune cells [45]. Thus, no existing studies have compared a large panel of cancer and normal cells, where commonalities and differences between GO interaction with diseased and healthy cells could be explored in-depth. Studies reporting GO uptake in cancer and normal cells have been contradicting [36, 37, 38, 39, 44, 45, 46]. Some studies showed the uptake of GO in both cancer and normal cells [38, 39, 44, 46], and others showed no uptake of GO in cancer and/or normal cells [36, 37, 45]. In some cases, GO is modified with different moieties to enhance cancer cell interaction compared to normal cells [37, 39]. One factor that may have added to the inconsistent findings is that some studies involved the attachment of labels to enable GO tracing and uptake detection in cells [36, 38, 46]. Consequently, the intrinsic properties of GO can be altered by the labelling process, and the risk of misinterpretation due to potential label detachment is also increased.

Furthermore, the selection of analytical techniques for the uptake assessment of GO is critical. Confocal laser scanning microscope (CLSM), transmission electron microscopy (TEM), and flow cytometry are three of the most common techniques used for cellular uptake assessments. However, each of these techniques has its advantages and shortcomings. Briefly, CLSM allows efficient distinguishment between internalised and cell surface adsorbed material in a time-efficient manner, but fluorescent labelling of material is often needed. TEM is an extremely powerful technique that offers high-resolution images, but it is a low throughput technique, so assessment by TEM is often restricted to a small sample size of cells. Also, considering that cellular compartments and GO are built mainly of carbon atoms, clear distinguishment between the material and cellular compartments is not always easily achieved. Finally, flow cytometry quantifies the total cellular interaction of material but cannot distinguish between internalised material and those adsorbed on cells. Thus, CLSM, TEM, and flow cytometry are good complementary techniques, but ambiguity could arise due to over-reliance on only one of these techniques, particularly flow cytometry. However, surprisingly, flow cytometry has been frequently used as a stand-alone or main analytical technique for assessing cellular uptake of GO [20, 21, 33, 42, 43, 44, 45, 46], leading to contradictory findings. For example, while both Yue et al. and Paino et al. investigated the uptake of non-functionalised label-free GO (with similar sizes) by flow cytometry, the former reported that cancer and normal cells (MCF-7, Hep G2, LLC, and HUVEC) were not able to internalise the material, but the latter reported the uptake of GO in both cancer and normal cells (HeLa, L929) [44, 45].

To close the identified research gap, we systematically compared the uptake of label-free, non-functionalised GO in a panel of cancer and normal cell lines combining CLSM, flow cytometry and TEM. Furthermore, we identified the properties of GO and cellular effects that influence the way GO interacts with cancer and non-cancer cells.

Result and discussion

Interactions of GO with cancer and non-cancer cells

GO-cellular interaction assessment by confocal imaging

We first assessed the cellular uptake of GO by confocal imaging. We used thoroughly characterized small-GO (s-GO, 25 nm–2.4 μm) and ultrasmall-GO (us-GO, 10–790 nm) in the present study (Figure S1, Table S1). Figure S2 shows the interaction of GO (s- and us-GO, 50 μg/mL) in NIH/3T3 (non-cancer) and HeLa (cancer) cells after 24 h of incubation by CLSM. Cellular uptake of GO is indicated by the localisation of the GO signal (in red) within the plasma membrane (stained green); internalised GO is shown as concentrated red spots localised towards the centre of the cell. On the other hand, extracellular GO interacting with the plasma membrane is shown as dispersed clouds of red signals surrounding or localised on top of cells. Interestingly, we identified two distinct GO interaction patterns between the two cell lines. In NIH/3T3, both s- and us-GO were found internalised and interacting with the plasma membrane, with no obvious differences in the uptake quantity. Meanwhile,

for HeLa cells, both s- and us-GO were found to interact with the plasma membrane, and no intracellular distribution of the materials was observed. This pattern agrees with the results from our previous study, where we observed the uptake of GO in the non-cancer cell lines [47]. The uptake of GO (s- and us-GO at 25, 50, and 75 μg/mL for 24 h) was then assessed in a total of eight cancer and five non-cancer cell lines by CLSM (Fig. 1, S3 – S14, and Table S2). Surprisingly, the non-cancer cells were repeatedly found to take up both s-GO and us-GO, but none of the cancer cell lines were found to take up the two materials. Further analysis in cancer (HeLa, LNCap, PC3) and non-cancer (BEAS-2B, NIH/3T3, PNT-2) cells showed the same interaction pattern remained for large-GO (l-GO, 1.5–25.5 μm) (Figure S15).

All studied cell lines were maintained in cell-type specific media either recommended by the American Type Culture Collection (ATCC) or previously determined experimentally. However, in all GO treatments (unless specified), the same cell culture media (RPMI-1640 with 10% FBS) was used to exclude variability induced by different media compositions. Despite literature reporting lower membrane penetration of GO upon coating with serum proteins, we previously demonstrated the uptake of GO *via* receptor-mediated pathways (e.g., clathrin-mediated endocytosis) [21, 47]. This provides evidence that the lack of GO uptake in cancer cells was not due to protein coronation in serum-containing environments hindering the binding of GO to membrane receptors.

To examine the effect of treatment media, we compared the uptake of GO in cancer cells under different treatment media. In human epithelial prostate carcinoma cells (DU 145), we observed no apparent changes in the uptake profile of GO (s- or us-GO) using RPMI-1640 (see Figure S12a) or DU 145 cells specific media (see Figure S12b). In agreement, human epithelial glioblastoma cells (U87 MG) also showed comparable GO interaction patterns using RPMI-1640 (see Figure S11) or U87 MG cell-specific media [48]. Therefore, the choice of treatment media was not the dominant factor driving the uptake difference of GO between cancer and non-cancer cells.

GO-cellular interaction assessment by TEM

To confirm the observations by CLSM, we next examined the uptake of GO using TEM (Fig. 2a – d). As expected, internalised GO was found within the vesicles of BEAS-2B and NIH/3T3 cells, with no obvious signs of cytosol localised GO flakes (Fig. 2a – b). In contrast,

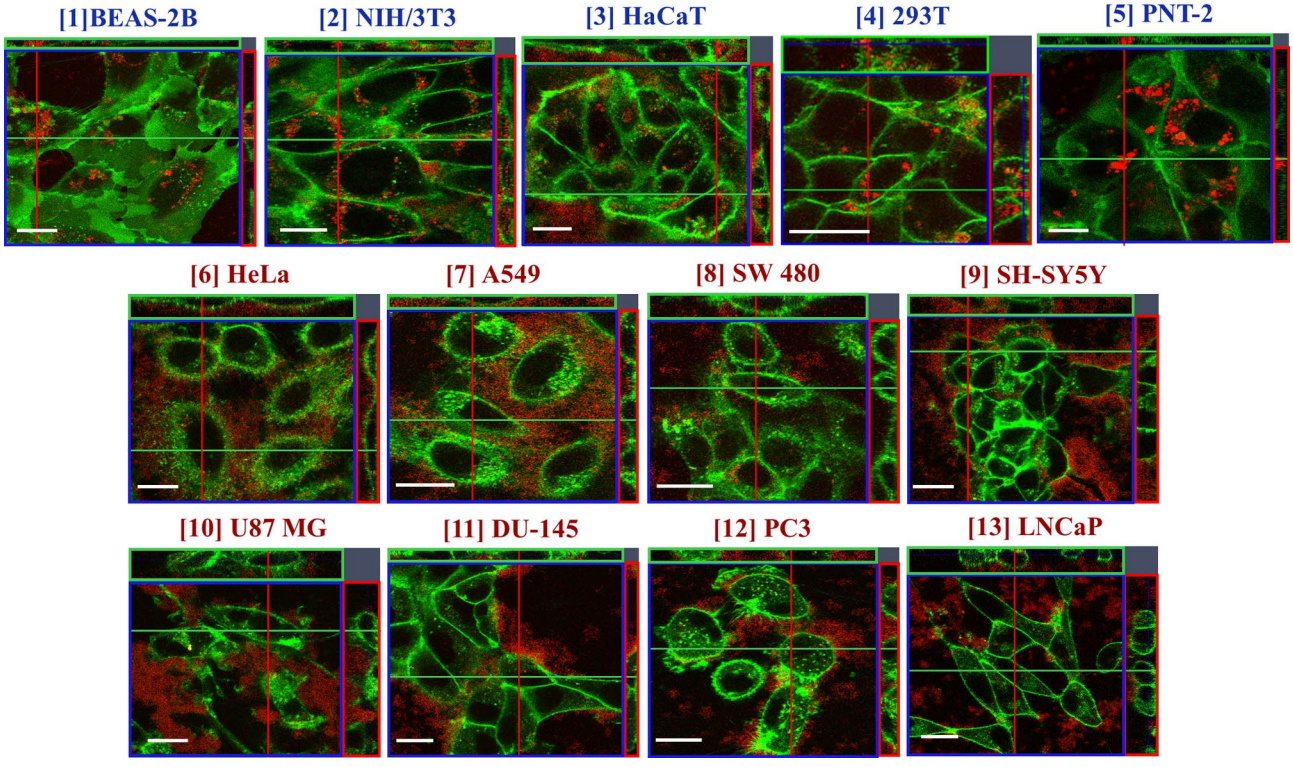

Fig. 1 Interaction of GO (s- and us-GO) in cancer and non-cancer cells, assessed by CLSM (orthogonal projections of the middle section of the cell are shown). Non-cancer cells: **[1]** BEAS-2B (s-GO treated), **[2]** NIH/3T3 (us-GO treated), **[3]** HaCaT (s-GO treated), **[4]** 293T (us-GO treated), **[5]** PNT-2 (s-GO treated). Cancer cells: **[6]** HeLa (s-GO treated), **[7]** A549 (us-GO treated), **[8]** SW 480 (s-GO treated), **[9]** SH-SY5Y (us-GO treated), **[10]** U87 MG (s-GO treated), **[11]** DU-145 (us-GO treated), **[12]** PC3 (s-GO treated), and **[13]** LNCaP (s-GO treated). See Figure S3–14 for the full panel of GO (s- and us-GO) interaction profiles in cell lines **[2]–[13]**, respectively. See Chen et al.47 for in-depth GO (s- and us-GO) interaction profiles and uptake mechanisms in **[1]** BEAS-2B cells. See Table S2 for the summary of GO (s- and us-GO) interaction profiles in all cell lines. Green = plasma membrane, Red = GO. Scale bar = 20 μm

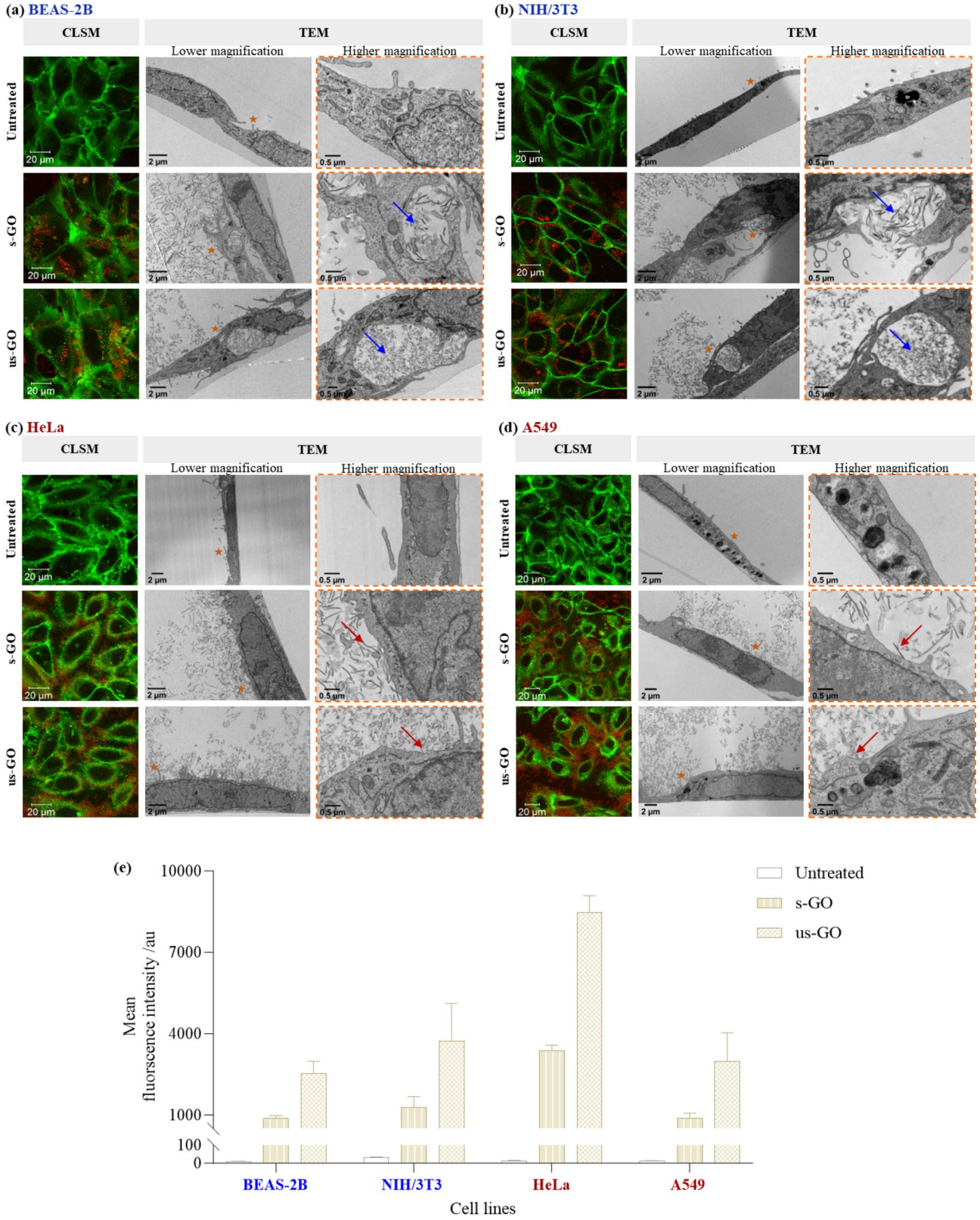

Fig. 2 Interaction of GO (s- and us-GO, 50 μg/mL) with **(a)** BEAS-2B, **(b)** NIH/3T3, **(c)** HeLa and **(d)** A549 cells by CLSM, TEM and **(e)** flow cytometry. For analysis by flow cytometry, the cells were collected with PBS (-/-) washing; see Figure S17 for cells collected without PBS (-/-) washing. See Table S3 for the corresponding statistical analysis of the GO-cellular interaction by flow cytometry. Green = plasma membrane, red = GO. For the TEM images, stars at lower magnification indicate the proximate area imaged for higher magnification; arrows at higher magnification indicate membrane-bound GO (blue arrows) or cell-surface interacting GO (red arrows)

most HeLa and A549 cells showed no sign of GO internalisation (Fig. 2c – d). Thus, this finding confirmed the uptake difference of GO in cancer and non-cancer cells, as identified by CLSM. However, we noticed that cancer cells attempted to take up the materials, as indicated by plasma membrane ruffling and deformations near GO (Figure S16). Also, although most of the s-GO and us-GO were found interacting with the cancer cell plasma membrane without being taken up, very few cancer cells were found with internalised small amounts of us-GO, localised within intracellular vesicles (Figure S16).

GO-cellular interaction assessment by flow cytometry

We further examined the cellular interaction of GO using flow cytometry, which quantifies the total interaction of GO with cells (i.e., the sum of GO taken up and adhered to the cells). The interaction of GO (s- and us-GO) with cancer (HeLa, A549) and non-cancer (BEAS-2B, NIH/3T3) cell lines were compared, with (Fig. 2e) and without (Figure S17) washing prior to flow cytometry examination. For both cancer and non-cancer cell lines, washing greatly reduced the mean fluorescent intensity (MFI) of GO (s- and us-GO), which confirmed the presence of GO bound to the cell surface (see Figs. 2e and S17). However, regardless of the types of GO and whether washing was performed, the MFI for HeLa cells was significantly higher than for the other three cell lines. In contrast, no significant differences were observed between A549, BEAS-2B and NIH/3T3 cells (see Table S3a and Figure S17).

As both HeLa and A549 cells clearly showed minimal uptake of GO by CLSM and TEM, we concluded that GO adhered to the surface of the cells contributed to the fluorescent signal measured by flow cytometry. The difference in MFI between HeLa and A549 cells demonstrates that GO adhered more strongly to the HeLa cell membrane than the A549 cell membrane (Fig. 2e). One possible explanation for the discrepancy could be attributed to the intrinsic difference in the plasma membrane composition of the cells. Depending on the specific membrane constituents and their local concentrations, the types and strengths of the interaction forces between GO and the cell membrane vary. For example, electrostatic and steric repulsion could arise between negatively charged GO and membrane regions rich in anionic phospholipids and glycocalyx (i.e., a carbohydrate enriched meshwork of lipids and proteins coating the cell surface), leading to the lower adherence of GO to cell membranes[49, 50].

The MFI for us-GO was significantly higher than s-GO in all studied cell lines, with and without washing (see Table S3b and Figure S17). Considering the spectrofluorometric analysis of the GO emission spectra showed that the intrinsic fluorescent intensity of s-GO was higher than us-GO (Figure S18), the finding suggests that us-GO was better adsorbed to the plasma membrane of the cells than s-GO. Despite this, cell-type specificity toward uptake of GO was observed regardless of the GO sizes (Figs. 2 and S15). Therefore, we excluded the effect of GO sizes being the dominant factor in driving the GO uptake differences between cancer and non-cancer cells.

GO-cellular interaction discussion

Previous studies have reported the interaction of non-functionalised label-free GO with cancer cells using flow cytometry [20, 21, 44]. Several studies concluded on the uptake of GO in A549 cells [20, 21], using flow cytometry [42, 43, 44, 46]. Thus, it is important to recognise that uncertainty could arise from the presence of extracellular bound materials in uptake studies mainly based on flow cytometry.

Likewise, the uptake of GO in cancer cells by TEM has been widely reported [5, 16, 22, 23, 40]. However, it is essential to acknowledge that the cell sample size analysed by TEM is relatively small compared to other techniques such as CLSM and flow cytometry. Therefore, uptake studies solely based on TEM can suffer from the overemphasis on the success or failure of the uptake but are rarely concerned with the level and scale of uptake.

Proceeding, our results showing successful uptake of GO in non-cancer cells are in agreement with the previous findings [28, 32, 36, 47]. However, the uptake of GO in non-cancer cells has been shown to depend on the cell phenotype [31]. For example, Kucki et al. showed that GO was internalised by undifferentiated intestinal cells but not the differentiated intestinal cells with hair-like surface structures [31]. Thus, cell surface topography that permits better association of GO with the plasma membrane allows enhanced GO uptake.

Interactions of other nanomaterials with cancer and non-cancer cells

Size, shape, and surface chemistry are the most extensively studied physico-chemical properties critical for nanomaterials (NMs)-cellular interaction. To explain the observed differential uptake of GO by cancer and non-cancer cells, we interrogated the capacity of cancer and non-cancer cells towards the uptake of NMs with different size, shape, and surface chemistry. The NMs used were divided into two groups: **(1)** commercially available polystyrene microspheres with different size and surface charge (negatively charged carboxylate-modified beads [0.1, 0.5, and 1 μm] and positively charged amine-modified beads [0.2 and 1 μm]), and **(2)** graphene flakes with different surface charge (negatively charged 1-pyrenesulfonic acid sodium salt stabilised graphene dispersion [Gr-PS1] and positively charged trimethylammonium linked pyrene stabilised graphene dispersion [Gr-TMA_3]). The

graphene flakes were produced and characterized as already described30, 51, 52.

Microspheres were selected because spheres are one of the most commonly used types of NMs [53], and they are typically better internalised than two-dimensional (2D) NMs [36]. By interrogating cellular capacity to take up microspheres of different sizes and functionality, we aimed to confirm if cancer cells, in general, have a lower endocytic ability than non-cancer cells or if this applies only to materials with specific properties. Second, using graphene flakes of different functionalities and surface charges, we aimed to confirm the ability of cancer cells to internalise other 2D NMs.

Microspheres-cellular interaction assessment

Figures 3 and 4 show the interaction of cancer and non-cancer cells with the FITC-labelled microspheres with positive (+) and negative (-) surface charge, assessed by CLSM and flow cytometry, respectively. Figures 3 and 4 showed that for both cancer and non-cancer cells, the uptake of the − 1 μm beads was comparable to the + 1 μm beads. However, BEAS-2B cells exhibited the highest uptake, followed by HeLa, NIH/3T3 and A549 cells as evidenced by normalised MFI values (MFI values were normalised against the intrinsic fluorescent intensity of the starting microspheres dispersion, see Figure S19): BEAS-2B (-1 μm = 16929, + 1 μm = 15005), HeLa (-1 μm = 4872, + 1 μm = 5119), NIH/3T3 (-1 μm = 4008, + 1 μm = 4114) and A549 (-1 μm = 3614, + 1 μm = 3603). Likewise, for both cancer and non-cancer cells, the uptake of -0.5 and − 0.1 μm beads exhibited a similar trend: the normalised MFI was highest in BEAS-2B cells (-0.5 μm = 4070, -0.1 μm = 1843), followed by NIH/3T3 (-0.5 μm = 1392, -0.1 μm = 662), HeLa (-0.5 μm = 992, -0.1 μm = 545) and A549 (-0.5 μm = 556, -0.1 μm = 344). On the other hand, the highest uptake of the + 0.2 μm beads was observed in HeLa cells (9303), followed by BEAS-2B (5228), A549 (4719) and NIH/3T3 (3437) cells (see Figs. 3 and 4).

Despite variability in the level of uptake, both cancer and non-cancer cells were able to internalise all the beads, regardless of their size or charge. Furthermore, the lack of significant difference in the uptake of 1 μm beads between NIH/3T3 cells and cancer cells (A549 and HeLa cells) demonstrates that cancer cells do not, intrinsically, exhibit a lower uptake capacity than non-cancer cells (see Figure S20 for statistical comparison between cancer and non-cancer cells). Similarly, the comparable uptake of -1 and + 1 μm beads in cancer cells indicates that they do not exhibit, intrinsically, a reduced capacity for internalising negatively charged materials (see Fig. 4). Moving on, both cancer and non-cancer cells were found to take up the small positively charged (+ 0.2 μm) beads better than the small negatively charged (-0.1 μm) beads. It is important to note that in both HeLa and A549 cells, the + 0.2 μm beads were most uptaken. Thus, the result suggests that the role of surface charge on the uptake of material, particularly in cancer cells, may become more significant for the material below a certain size.

Graphene flakes-cellular interaction assessment

We next investigated the uptake of Gr-TMA_3 and Gr-PS1 in cancer (HeLa) and non-cancer (BEAS-2B) cells by CLSM (Figure S21a-b) and flow cytometry (Figure S21c). As shown in Figure S21a-b, due to the light absorption properties of graphene flakes, the material appears black in the bright field channel. On the other hand, the cell was stained green with the fluorescein diacetate (FDA) dye, and where the cell had taken up the material, the flakes quenched the signal of the dye. It is apparent from Figure S21a-b and Figure S21c that the results obtained using CLSM and flow cytometry are in agreement. Both Gr-TMA_3 and Gr-PS1 were internalised in BEAS-2B and HeLa cells, which confirms that cancer cells could take up positively or negatively charged 2D NMs. However, the positively charged Gr-TMA_3 were internalised better than the negatively charged Gr-PS1 flakes in both BEAS-2B (side scattering fold change with respective to untreated cells: Gr-PS1 = 1.07, Gr-TMA_3 = 1.81) and HeLa (side scattering fold change with respective to untreated cells: Gr-PS1 = 0.57, Gr-TMA_3 = 1.18) cells. Considering that graphene flakes had an average size of approximately 200 nm [30], this is in line with results from the uptake study of the microspheres, where the small positively charged microspheres were taken up better than the small negatively charged ones (see Figs. 3 and 4). However, BEAS-2B cells were noticeably taking up both Gr-TMA_3 and Gr-PS1 better than HeLa cells (see Figure S21). This is different from those observed from the uptake study of the microspheres, where the small positively charged microspheres were taken up better in HeLa cells than BEAS-2B cells (see Figs. 3 and 4). Thus, the result suggests that the uptake of 2D NMs is not solely driven by the combined role of surface charge and size.

Implications of the findings on understanding GO-cellular interaction

Findings from the uptake study of microspheres and graphene flakes demonstrate that the material surface charge affects its uptake in cancer and non-cancer cells, but not in an "all or nothing" manner. As is well-known, the material surface charge affects the electrostatic interactions between the material and plasma membrane [54]. Positively charged NMs have been reported to internalize better than their negatively charged counterparts due to a more energetically favourable interaction with the cell surface that enhances the endocytosis process [54, 55].

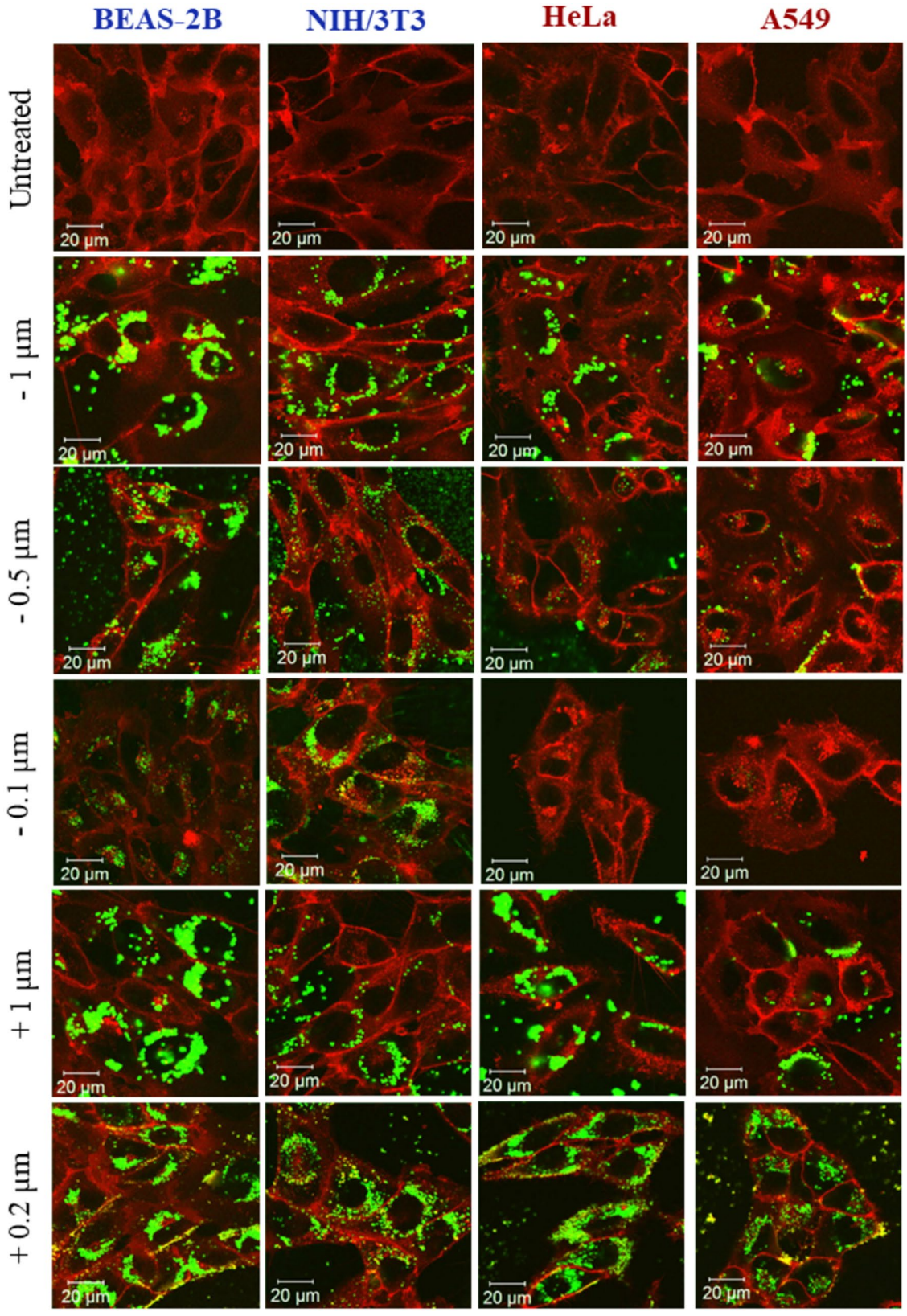

Fig. 3 Interaction of BEAS-2B, NIH/3T3, HeLa and A549 cells with negatively charged (–) 0.1, 0.5, and 1 µm carboxylate-modified, and positively charged (+) 0.2 and 1 µm amine-modified beads by CLSM. Red = plasma membrane, green = FITC-labelled beads. Scale bar = 20 µm

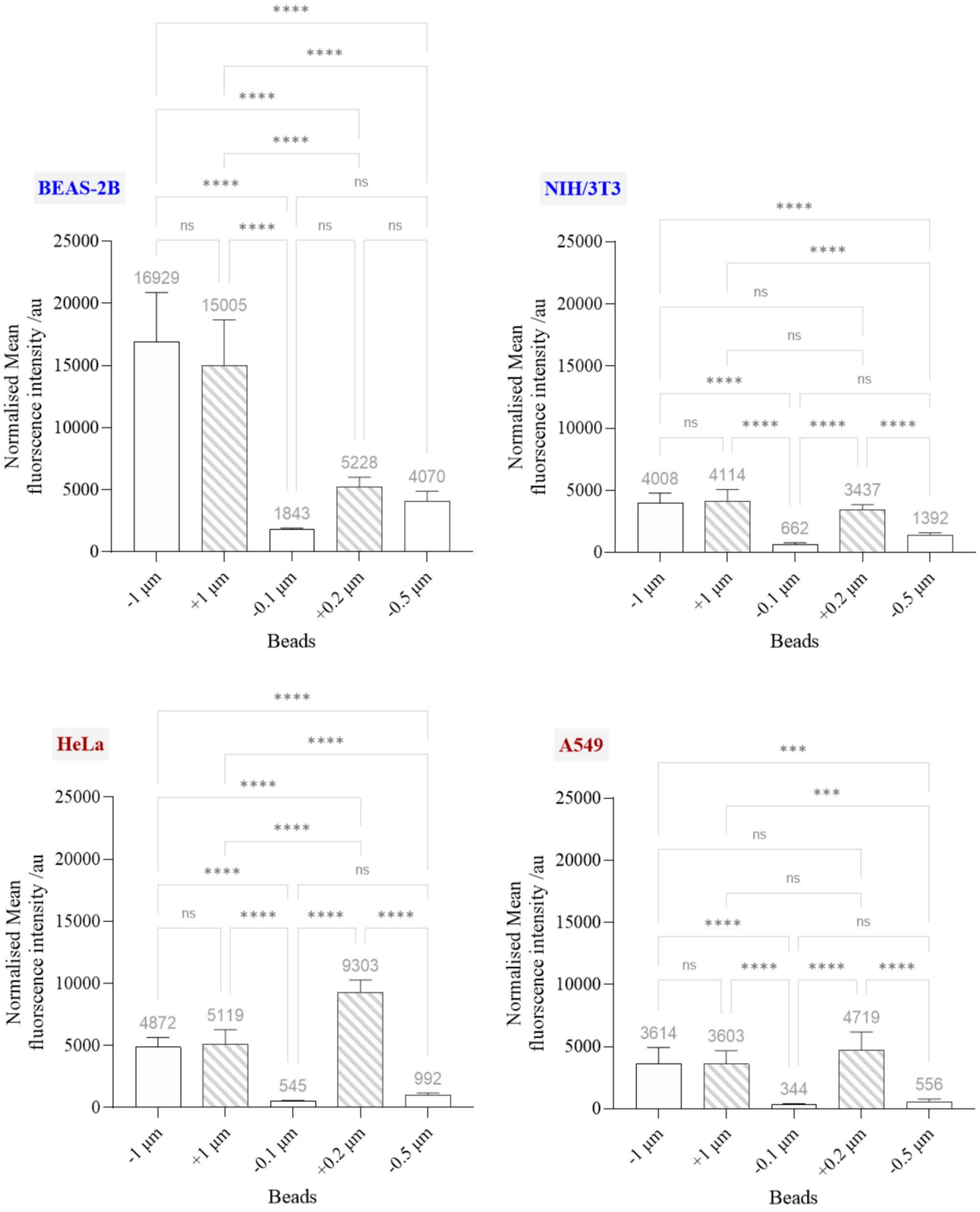

Fig. 4 Interaction of BEAS-2B, NIH/3T3, HeLa and A549 with negatively charged (–) 0.1, 0.5, and 1 µm carboxylate-modified, and positively charged (+) 0.2 and 1 µm amine-modified beads by flow cytometry. The raw data were normalised against the microsphere with the lowest intrinsic fluorescent intensity at 515 nm (see Figure S19 for the emission spectra of the microspheres). The normalised data were statistically analysed using analysis of variance (one-way ANOVA) with Tukey's multiple comparisons test. $n = 3$ with duplicates. *Statistically different: ***$p < 0.001$ and ****$p < 0.0001$. ns = not significant

Indeed, it has been suggested that the lack of GO uptake in non-phagocytic cells is due to the electrostatic repulsion between the material and plasma membrane [45]. However, we observed GO interaction with both cancer and non-cancer cell plasma membranes, and our result by flow cytometry demonstrate that GO adhered strongly to the cancer cell surface (Figs. 1 and 2, and S2–17). In fact, the adhesion of GO on the plasma membrane of cancer cells has been widely acknowledged by different research groups [21, 24, 32, 41].

It is worth noting that GO may interact more with the cancer cell plasma membrane than the microspheres/graphene flakes. As shown by CLSM (Figure S2, the middle section of cells), GO was displayed as a uniform cloud of signal surrounding the HeLa cell plasma membrane, outlining the shape of HeLa cells. In comparison, substantially fewer microspheres/graphene flakes were found surrounding the HeLa cell plasma membrane (Figs. 3 and S21). The difference in material thickness may have contributed to the difference between GO and the microspheres/graphene flake in the plasma membrane interaction. Being mostly monolayer, over 90% of the GO sheet had a thickness of 2 nm or less (see Table S1). In contrast, while the microspheres had a thickness range of 0.2–1 μm, the graphene flakes existed mostly as few-layers graphene (70 and 61% for Gr-TMA_3 and Gr-PS1, respectively) with a thickness range of 2–20 nm [30, 51, 52].

Previous research into the effect of Gr thickness by simulation showed that few-layer graphene (3 or 9 layers) exhibited an increase in the energy barrier for piecing the lipid bilayer compared to the single-layer graphene [56]. It can be expected that thickness influences the specific surface area by volume of the material, and these differences can directly affect the colloidal behaviour of the material, which ultimately results in the formation of different biological interfaces when interacting with cells [57]. Thus, despite its two-dimensionality, the colloidal behaviour of graphene flakes may share commonality with the three-dimensional microspheres, contributing to a more similar pattern of cellular interaction. In contrast, the thinner GO possess greater two-dimensionality and remains as individualised 2D sheets when interacting with cells, as shown by TEM (see Fig. 2).

Taken together, we clearly demonstrated that cancer cells take up materials with diverse properties, including shape, size, or surface charges comparable to GO. However, neither the uptake of microspheres nor the graphene flake occurs in the cell-type specific manner as observed for GO. We therefore conclude that the difference in thickness between GO and microsphere/graphene flakes could contributes to the cell-type specific uptake of GO.

Effects of GO on endocytosis-relevant biological properties of cells

The effect of GO on actin filaments

It was reported that GO could induce biological changes in cells, such as alteration of the plasma membrane composition [58], cytoskeleton [13, 20, 41, 59] and migratory ability of cells [19, 60]. Therefore, we asked if GO induces differential changes in endocytosis-relevant biological properties of cancer and non-cancer cells, ultimately contributing to the observed differences in GO uptake.

The effect of GO on cytoskeleton was examined by actin filament staining. Remodelling of the cytoskeleton is a prerequisite for endocytosis [61, 62]. In particular, actin filaments are crucial for all three major uptake pathways [63]; actin filaments disruption agents such as latrunculins and cytochalasin D are well-known pharmaceutical inhibitors of endocytosis [64].

Figure 5 and Figure S22 show the actin filament network for BEAS-2B and HeLa cells with and without GO (s- or us-GO, 100 μg/mL, 24 h), stained using the Alexa-Fluor 488-labelled phalloidin (Figure S23 for NIH/3T3 and A549 cells). In addition, methyl-beta-cyclodextrin (MβCD), which disrupts the cytoskeleton by depletion of the cholesterol in the cell membrane, was used as the positive control. Images in Figs. 5, S22 and S23 are shown in the range indicator mode to better compare the actin filament network. The images are displayed in black and white, with red and blue areas. Red and blue represent areas with saturated and zero intensity, respectively. At the same time, black and white colours represent lower and higher intensity areas, respectively. The settings were adjusted to display the background in blue, and the same intensity settings were applied within each cell line.

For all four cell lines, it is apparent that MβCD induced significant disruption to the actin filament network, resulting in an altered cell morphology compared to the untreated cells (see Figs. 5, S22 and 23). In general, MβCD treated cells appeared smaller than the untreated cells. In addition, features including the loss of the parallel distribution of the filaments, formation of actin spots, fragmented fibres, and increased stress fibres can also be identified in MβCD treated cells. On the other hand, the result showed that GO (s- and us-GO) could induce changes to the actin filament network in cancer cells, but no apparent differences were noted in the non-cancer cells (see Figs. 5, S22 and 23). One observed similarity in the effect of GO (s- and us-GO) on HeLa and A549 cells was that the actin filament density appears to be reduced in the GO treated cells compared to the untreated cells, shown by the increased lower intensity areas in GO treated cells (see Figs. 5, S22 and 23). However, neither s-GO nor us-GO in HeLa or A549 cells could induce changes to a level comparable to MβCD,

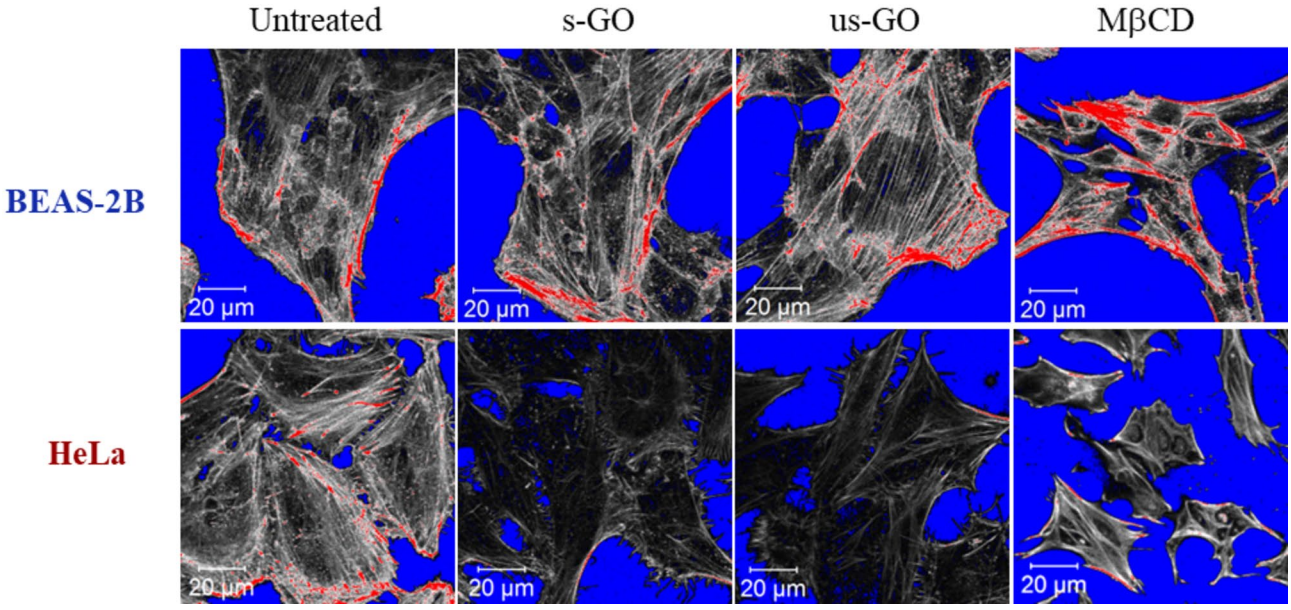

Fig. 5 Staining of actin filament in BEAS-2B and HeLa cells, treated with and without GO (s-GO or us-GO at 100 μg/mL, 24 h) or MβCD (5 mM, 4 h, positive control). Cells were stained with the phalloidin 488 dye for actin filament, and the images are shown in the range indicator mode: red and blue represent saturated and zero intensity areas, whereas black and white represent lower and higher intensity areas, respectively

where a pronounced reduction in the shape and size of cells was observed.

The actin cytoskeleton is heavily involved in many endocytic pathways, including clathrin-mediated endocytosis (CME), caveolae-mediated endocytosis (CavME) and macropinocytosis [64]. Notably, we previously confirmed GO internalisation in BEAS-2B cells *via* these three pathways [47]. Furthermore, disruption to the organisation and dynamic of the actin cytoskeleton has been widely recognised as the effect of various endocytosis inhibitors [64]. Hence, this result provides some tentative initial understanding of the observed GO uptake difference between cancer and non-cancer cells. Yet, the finding raised the intriguing question regarding the underlying mechanism for the remodelling of the actin cytoskeleton by GO and the selectivity toward cancer cells.

In agreement with the present results, previous studies have reported the reduction of the actin filament density in cancer cells with GO treatment [20, 41]. It has been suggested that GO impairs the cytoskeleton by direct interaction [20, 65] or indirectly through suppression of the cell adhesion system [41]. Tian et al. and Bera et al. suggested the direct interference of GO with the actin filament and microtubule network in A549 and HCT116 cancer cells, respectively [20, 65]. However, in these studies, the main evidence for GO's direct interference with the cytoskeleton was based on GO incubation with the isolated actin filaments and tubulin protein. In our study, for cancer cells, GO was found predominantly surrounding the plasma membrane and not being available to directly interact with actin filaments in the cytosol.

In the study by Zhu et al., GO impaired the plasma membrane and lowered integrin expression in A549 cells, which subsequently affected the cell adhesion complex and the cytoskeleton network [41]. A growing body of evidence demonstrates that changes in cell biomechanical properties induce actin cytoskeleton reorganisation and modulate the uptake of nanoparticles [66, 67, 68, 69]. For example, higher uptake of nanoparticles was observed for cells seeded on stiffer substrates [67, 68]. Furthermore, substrate stiffness has been reported to regulate cell stiffness, with cell softening and reduced actin polymerisation observed for cells seeded on softer substrates [70]. Considering the growing amounts of evidence that shows cancer cells are softer than normal cells in 2D cultures [71], and findings that show GO can modulate cancer cell mechanical properties by reducing cell stiffness and inducing actin cytoskeleton remodelling [72], one possible hypothesis is that GO acts as mechanical cues that prompt further softening of cancer cells, resulting in cytoskeletal reorganisation, and ultimately affecting the endocytosis of GO.

Furthermore, recognising the close association of actin filament with the plasma membrane provides valuable insights into the potential underlying mechanism for the disruptive effects of GO on cancer cell actin filament. For example, membrane phospholipids, such as phosphatidylinositol derivatives (e.g., phosphatidylinositol 4,5-bisphosphate and phosphatidylinositol

(3,4,5)-trisphosphate), are indispensably involved in the actin dynamics regulation by modulating the availability of free actin monomers and the activity of various key actin-binding proteins [73]. Disruption to plasma membrane composition (e.g., cholesterol depletion by MβCD) or interference with its highly regulated activity (e.g., by blocking the binding site of phosphatidylinositol 4,5-bisphosphate with pleckstrin homology domains) induce cytoskeletal reorganization [74]. Inspired by evidence of GO-induced alteration in the lipid composition of the plasma membrane, and the evidence of cancer cells suggesting elevated levels of phosphatidylinositol and cholesterol than their normal counterpart, it is possible to hypothesis that cancer cells is more responsive to GO-plasma membrane interaction [58,75, 76]. Thus, this in turn, translate into the global effects on cell cytoskeleton. Nevertheless, we should bear in mind that GO did not induce actin filament disruption to the same extent as MβCD. Hence, the GO-plasma membrane interaction mechanism is likely less destructive.

The effect of GO on cell migration

Subsequently, the effect of GO on cell migration was investigated to validate its effect on actin filaments. Like endocytosis, regulation of the cytoskeleton network is essential for cell migration [77, 78]. Therefore, the disruption of the actin cytoskeleton will affect cell migration. For instance, pharmaceutical inhibitors such as cytochalasin B, which disrupt actin filament polymerisation, inhibit cell migration as well as endocytosis [79, 80]. We employed time-lapse tracking to assess the effect of GO on cell migration.

Herein, HeLa (one of the most studied cancer cell lines for GO cellular interaction) and BEAS-2B cells were used as representatives of cancer and non-cancer cell lines. BEAS-2B was chosen because we have previously established the uptake mechanism of GO in BEAS-2B cells [47]. In Fig. 6, we compared migratory differences between untreated cells and cells treated with s-GO (50 μg/mL). Using cell trajectories, we observed that for both BEAS-2B and HeLa cells, untreated cells moved in a larger spreading area than cells treated with s-GO (see Fig. 6a). However, the difference between the observed

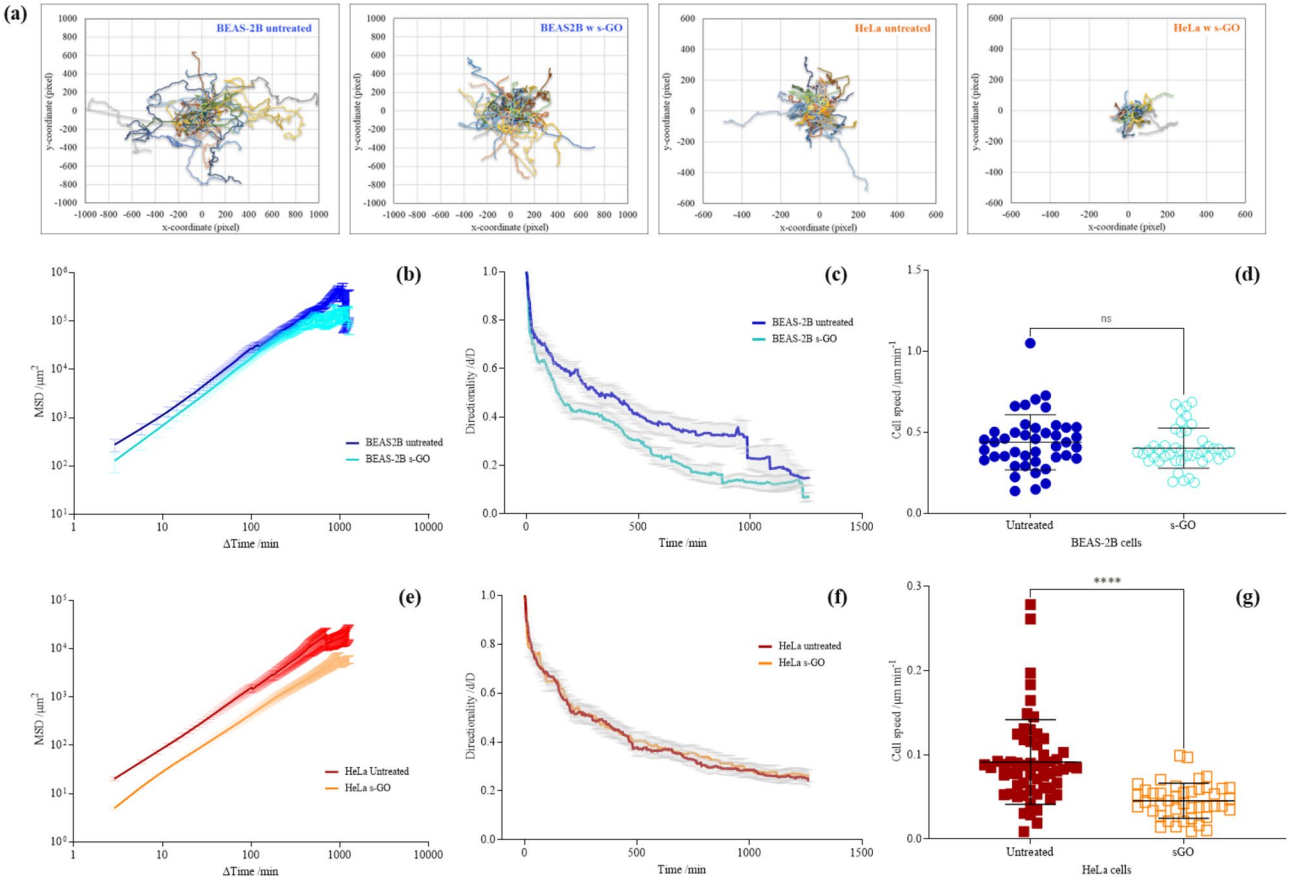

Fig. 6 The effect of GO (50 μg/mL) on **(a** – **d)** BEAS-2B and **(a**, **e** – **g)** HeLa cell migration, assessed by live cell time-lapse tracking. Cell trajectories are visualised *via***(a)** plot at the origins and further analysed *via***(b**, **e)** MSD, **(c**, **f)** directionality analysis, and **(d**, **g)** cell speed measurement. Cell speeds are statistically analysed using an unpaired T-test. Number of cells analysed per condition = 43. *Statistically different: ****$p < 0.0001$, ns = not significant

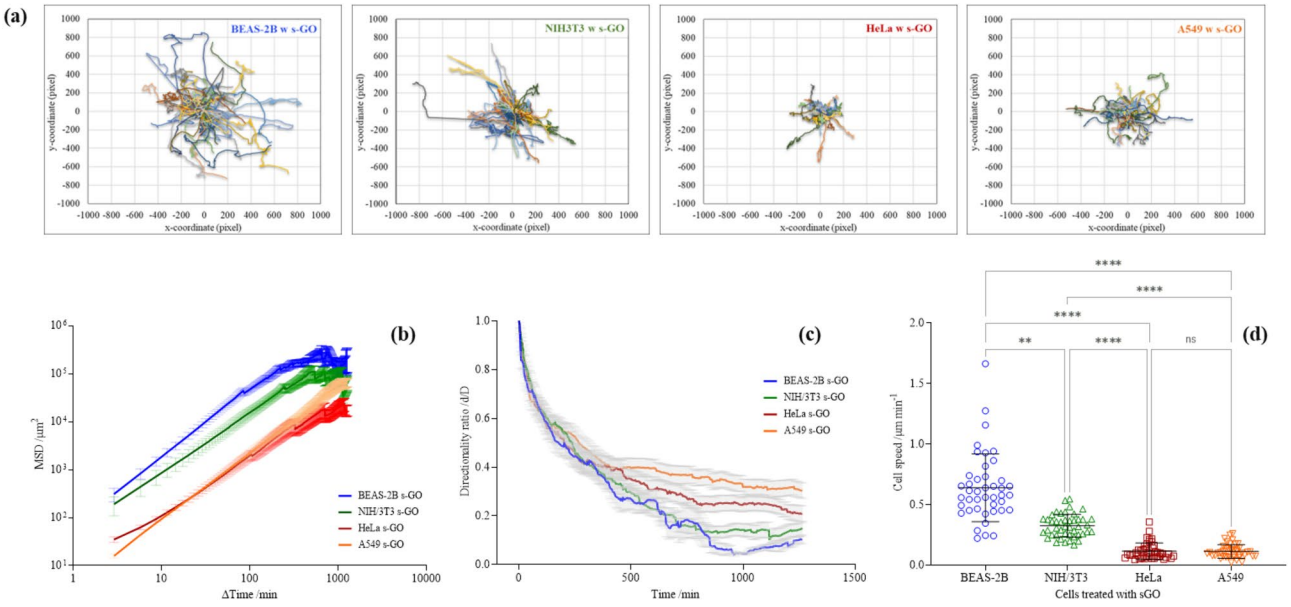

Fig. 7 Comparison of cancer (HeLa, A549) and non-cancer cells (BEAS-2B, NIH/3T3) migration when interacting with s-GO (50 μg/mL). Cell trajectories are visualised *via* **(a)** plot at the origins and further analysed *via* **(b)** MSD, **(c)** directionality analysis, and **(d)** cell speed measurement. Cell speeds were statistically analysed using analysis of variance (one-way ANOVA) with Dunn's multiple comparisons test. Number of cells analysed per condition ≥ 43. *Statistically different: $^{**}p < 0.01$, $^{****}p < 0.0001$, ns = not significant

effect was greater for HeLa than BEAS-2B cells. This observation was further supported by the mean square displacement (MSD) measurement (see Fig. 6b and e), where the average surface area used by cells was plotted over time [81].

To understand better the effect of s-GO on BEAS-2B and HeLa cells, we further examined two key parameters that account for cell migration efficiency: directionality persistence and cell speed [81]. In Fig. 6c and f, the average directionality ratio over time is shown. The directionality ratio (d/D) for a set time point is the ratio of the straight-line distance (d) from the cell's initial to end positions at the set time point over the actual distance (D) the cell travelled. Hence, if the directionality ratio equates to one, it suggests the cells have followed a perfectly straight path, whereas if the ratio approaches zero, it means the cells have followed a highly curved path. However, it should be noted that, in the absence of migration cues, directionality persistence for randomly moving cells will decay and vary considerably over time [81]. Therefore, instead of comparing the directionality ratio at one set time point (e.g., at the endpoint), assessing the directionality ratio over the time course better represents directional persistence.

As shown in Fig. 6c, the BEAS-2B untreated cells followed a straighter path than s-GO treated BEAS-2B cells. This is shown by the rapid decay of the directionality curve in s-GO treated cells (mean d/D: 0.236 ± 0.008) compared to untreated cells (mean d/D: 0.402 ± 0.008). Whereas for HeLa untreated and s-GO treated cells, no apparent differences in the directionality ratio were observed over time (see Fig. 6f). The directionality curve for HeLa untreated (mean d/D: 0.359 ± 0.006) and s-GO treated (mean d/D: 0.372 ± 0.006) cells stay overlapped over the entire time course of cell trajectory. On the other hand, the HeLa cell speed reduced significantly with s-GO treatment, but comparable cell speeds were found for BEAS-2B cells with or without s-GO treatment (see Fig. 6d and g, respectively). For example, the average speed for HeLa untreated cells was 0.091 ± 0.050 μm/min, which was reduced by 50.5% in s-GO treated cells (0.045 ± 0.021 μm/min). In contrast, only an 8% difference was found in the average speed between BEAS-2B untreated (0.438 ± 0.170 μm/min) and treated (0.403 ± 0.124 μm/min) cells.

The observed effect on the speed and spreading area of s-GO treated HeLa cells supports the finding that GO induced actin filament disruption in this cell line. Also, what stands out from the result is that s-GO affected the migration of BEAS-2B and HeLa cells differently, with the directional persistence lowered in the former and the cell speed reduced in the latter. The result showed that the effect of s-GO on cell migration was also cell-line specific, further supporting the hypothesis that GO induces differential biological changes in cancer and non-cancer cells.

In addition, as shown in Fig. 7, we directly compared the migratory ability between BEAS-2B, NIH/3T3, HeLa and A549 cells when interacting with s-GO (50 μg/mL). The non-cancer cells exhibited a larger spreading area

compared to the cancer cell lines, with BEAS-2B cells exploring the widest territory, followed by NIH/3T3, A549 and HeLa cells (Fig. 7a). This agrees with the MSD plot (Fig. 7b). Furthermore, HeLa and A549 cells displayed a higher directional persistence than BEAS-2B and NIH/3T3 cells. The mean directionality ratio for HeLa and A549 cells was 0.382 ± 0.005 and 0.322 ± 0.006, whereas for BEAS-2B and NIH/3T3 cells was 0.263 ± 0.010 and 0.260 ± 0.008, respectively (Fig. 7c). In contrast, BEAS-2B and NIH/3T3 cells displayed a higher cell speed than the A549 and HeLa cells when interacting with s-GO (Fig. 7d). For example, the average speed for BEAS-2B and NIH/3T3 cells was 0.640 ± 0.280 and 0.327 ± 0.093 μm/min, respectively. In comparison, the speed for HeLa and A549 cells was 0.117 ± 0.068 and 0.114 ± 0.056 μm/min, respectively.

Taken together, direct comparisons of the migratory ability between BEAS-2B, NIH/3T3, HeLa and A549 cells confirmed that a greater effect of GO on cancer cell migratory ability than non-cancer cells (see Fig. 7b). BEAS-2B and NIH/3T3 non-cancer cells followed a more curved cell path and moved faster than the HeLa and A549 cancer cells when interacting with s-GO. This result supports GO induced actin filament disruption in cancer cells and further illustrates differences between cancer and non-cancer cells when interacting with the material. Consistent with our result, studies have reported the ability of GO to retard cell migration [13, 20, 41, 60]. However, most of these studies were performed only on cancer cells and lacked systematic comparison with non-cancer cells. Considering GO localised mostly extracellularly to cancer cells but was able to induce intracellular (see Fig. 5, S22 and S23), and behaviour (see Fig. 6) changes in cancer cells, elucidating the complex linkage between GO and cancer cells provides a novel opportunity to advance the understanding of manipulating cancer cells with extracellularly localised GO.

Conclusion

We systematically compared interactions of non-labelled, thin GO flakes with eight cancer and five non-cancer cell lines using a mix-method approach (CLSM, TEM, flow cytometry). Large, small and ultra-small GO flakes were found to predominately interact with the plasma membrane of cancer cells, rather than being internalised. Efficient uptake of GO is reported in all studied non-cancer cell lines.

We explored factors that drive cell-type preference towards GO uptake, including material properties and the effect of GO on endocytosis-relevant biological properties of the cell. Uptake of other materials, including polystyrene microspheres and graphene flakes with various sizes and surface charges, reveals that all were internalised by cancer (HeLa, A549) and non-cancer (Beas-2B, NIH/3T3) cells. This confirmed that cancer cells could take up different NMs, including thicker graphene flakes, suggesting the role of GO thinness in the observed uptake differences. Furthermore, we showed that GO induced actin cytoskeleton (a key player in endocytosis) disruption in cancer but not in non-cancer cells, is leading to differential changes in the migratory behaviour of cancer cells.

Our results reveal that an interplay between properties of GO and actin cytoskeleton disruption contributed to the observed uptake differences between cancer and non-cancer cells. This work invites further studies to explore the effects of GO on plasma membrane of cancer cells, potentially translating into an opportunity towards extracellular cancer cell manipulation using GO and plasma membrane targeted biomedical applications.

Experimental

Materials characterisation

Aqueous suspensions of large (l-GO), small (s-GO), and ultrasmall (us-GO) GO sheets were produced in house, and fully characterised, as previously described in Rodrigues et al. [3]. GO stock suspensions prepared in water for injection and under endotoxin-free conditions, and the same batch has been already used in Loret et al. [82]. Emission spectra of GO (s- and us-GO, 2 mg/mL) were acquired using Cary Eclipse fluorescence spectrophotometer (Varian Inc., Agilent Technologies, UK) at room temperature. GO was prepared in Milli-Q water or cell culture medium (RPMI with 10% FBS). GO prepared in cell culture medium was washed by centrifugation (30 min, 13 000 rpm, x 2, re-suspension in Milli-Q water) and re-suspended in Milli-Q water for measurement (excitation wavelength = 525 nm, blank = Milli-Q water). Graphene dispersion (Gr-TMA_3 and Gr-PS1) were kindly provided by Professor Ciniza Casiraghi (University of Manchester). Full production and characterisation of Gr-TMA_3 and Gr-PS1 can be found in Shin et al. and Yang et al. [30, 51, 52]. Emission spectra of the positively or negatively charged beads (F8765, F8764, F8823, F8813, F8803, Thermo Scientific, UK) were prepared and measured in cell culture medium (1.5 uL/mL, RPMI with 10% FBS, room temperature), using CLARIOstar Plus plate reader (BMG Labtech) with excitation wavelength = 472 nm.

Cell culture

Thirteen immortalised cell lines were used in this study. This includes five normal cell lines and eight cancer cell lines. (1) Human epithelial bronchial cells (BEAS-2B, CRL-9609, ATCC, LGC standards, UK), (2) human prostate epithelial cells (PNT-2, kindly provided by Professor Anna Nicolas, University of Manchester), and (3) human prostate carcinoma cells (LNCaP, kindly provided by Professor Anna Nicolas, University of Manchester) were

maintained in RPMI-1640 cell culture medium (R8758, Sigma-Aldrich, Merck Sigma, UK). (4) Human epithelial colon adenocarcinoma cells (SW 480, CCL-228, ATCC, LGC standards. UK) were maintained in advanced RPMI-1640 cell culture medium (R8785, Sigma-Aldrich, Merck Sigma, UK). (5) Mouse fibroblast embryonic cells (NIH/3T3, CRL-1658, ATCC, LGC standards, UK), (6) human epithelial keratinocyte cells (HaCaT, PCS-200-011, ATCC, LGC standards, UK), (7) human epithelial embryonic kidney cells (293T, CRL-2316, ATCC, LGC standards, UK), (8) human epithelial cervical adenocarcinoma cells (HeLa, CCL-2, ATCC, LGC standards, UK), and (9) human epithelial glioblastoma cells (U87 MG, HTB-14, ATCC, LGC standards, UK) were maintained in DMEM cell culture medium (D6429, Sigma-Aldrich, Merck Sigma, UK). (10) Human epithelial lung carcinoma cells (A549, CCL-185, ATCC, LGC standards, UK), and (11) human epithelial prostate adenocarcinoma cells (PC3, CRL-1435, ATCC, LGC standards, UK) were maintained in F-12 Ham cell culture medium (N6658, Sigma-Aldrich, Merck Sigma, UK). (12) Human epithelial prostate carcinoma cells (DU 145, HTB-81, ATCC, LGC standards. UK), and (13) human epithelial bone marrow neuroblastoma cells (SH-SY5Y, CRL-2266, ATCC, LGC standards, UK) were maintained in EMEM cell culture medium (M4655, Sigma-Aldrich, Merck Sigma, UK). All the cell lines except for LNCaP cells, were supplemented with 10% FBS, 1000 units Penicillin, and 1 mg/mL Streptomycin. LNCaP cells were supplemented with 10% hyclone FBS, 1 mM sodium pyruvate and 10 mM of HEPES solution. The cells were maintained at 37 ºC in a humidified 5% CO_2 incubator. Cells were split at 80% confluence with 0.05% Trypsin-EDTA (Sigma-Aldrich, Merck Sigma, UK), and 10% FBS (or hyclone FBS for LNCaP cells) was used to stop the activity of Trypsin-EDTA.

Cell culture treatments

Cells were seeded in Cellview™ dishes, 12-well plates, or 24-well plates with Aclar for experiments by confocal microscopy, flow cytometry, and TEM, respectively. Cells were always seeded in the cell-type specific medium for at least 24 h before treatments and treated when the cells reached 60–80% confluence (unless specified). In all treatment condition, RPMI-1640 cell culture medium (unless specified) supplemented with 10% FBS, 1000 units Penicillin, and 1 mg/mL Streptomycin were used as the pre-treatment and treatment medium and maintained at 37 ºC in a humidified 5% CO_2 incubator.

Confocal microscopy

Uptake of GO Cells were treated with GO (l-GO at 50 μg/mL, s-GO and us-GO at 25, 50, and 75 μg/mL, 0.5 mL/well, 24 h), after removal of cell supernatant, stained with the CellMask™ green plasma membrane dye (C37608, Thermo Fisher Scientific, UK) in the fresh treatment medium with a dilution of 1:2500, and imaged by Zeiss 780 CLSM using the 40X objective. Zeiss microscope software ZEN was used to process all the images. Excitation/emission wavelength: CellMask™ green = 488/520, GO = 594/620–690 nm.

Uptake of the beads Cells were treated with the positively charged (+ 1 μm and + 0.2 μm) or negatively charged (−1 μm, −0.5 μm and −0.1 μm) beads (1.5 μL/mL, 0.5 mL/well, 24 h, F8765, F8764, F8823, F8813, F8803, Thermo Scientific, UK, respectively), after removal of cell supernatant, stained with CellMask™ deep red plasma membrane dye (C10046), Thermo Fisher Scientific, UK) in the fresh treatment medium with dilution of 1:2500, and imaged by Zeiss 780 CLSM using the 40X objective. Zeiss microscope software ZEN was used to process all the images. Excitation/emission wavelength: CellMask™ deep red = 649/666, beads = 505/515 nm.

Uptake of graphene flakes Cells were treated with the positively charged (Gr-TMA_3) or negatively charged (Gr-PS1) graphene flakes (50 μg/mL, 0.5 mL/well, 24 h), just before imaging, cell supernatant removed and stained with Fluorescein Diacetate live cell dye (100 nM, 0.5 mL/well, Thermo Fisher Scientific, UK) in the fresh treatment medium, and imaged by Zeiss 780 CLSM using the 40X objective. Zeiss microscope software ZEN was used to process all the images. Excitation/emission wavelength: FDA = 488/520 nm.

Time-lapse tracking: untreated vs. s-GO treated cells BEAS-2B or HeLa cells were seeded in the Cellview™ dish and treated with s-GO (50 μg/mL, 0.5 mL/well) containing CellMask™ green plasma membrane stain (C37608, Thermo Scientific, UK). Live-cell time lapse was recorded within 1 h after the addition of GO treatment for 21 h, using Zeiss 780 CLSM (40X objective, time lapse mode). The videos were then extracted using Zeiss microscope software ZEN with the compression ratio of 20 and frames per second of 10. Excitation/emission wavelength: CellMask™ green = 488/520, GO = 594/620–690 nm.

Time-lapse tracking: cancer vs. non-cancer cells when interacting with s-GO BEAS-2B, NIH/3T3, HeLa and A549 cells were seeded in the same Cellview™ dish and treated with s-GO (50 μg/mL, 0.5 mL/well) containing CellMask™ green plasma membrane stain (C37608, Thermo Scientific, UK). Live-cell time lapse was recorded within 1 h after the addition of GO treatment for 21 h, using Zeiss 780 multiphoton CLSM (40X objective, time lapse mode). The videos were then extracted using

Zeiss microscope software ZEN. Excitation/emission wavelength: CellMask™ green = 488/520, GO = 594/620–690 nm.

Time-lapse tracking: video processing and analysis To obtain the cell trajectory information, cells were tracked manually using the CellTracker (version 1.1) software [83]. Briefly, the extracted video of live-cell time lapse by Zeiss 780 multiphoton CLSM was loaded onto CellTracker as Bio-Format images. Then, using the manual tracking option, the position of individual cell was manually defined by user clicking on the cell at every image frame until cell leave the frame; ≥ 43 cells were analysed in every conditions. Afterward, the statistic tap in CellTracker was selected, user defined manually the pixel size of frame (0.209 µm/pixel) and the time elapsed between subsequent frames (2.88 min/frame) according to the predefined setting of the recorded time lapse. The average cell speeds (µm/min) and individual cell trajectory (defined as *xy*-coordinate in each image frame) were extracted using the statistic function from CellTracker. Subsequently, the computed *xy*-coordinates data from the CellTracker were further analysed using the DiPer programme [81] to generate the plot at the origin, MSD curve, and directionality curve. Briefly, the pre-written program codes for DiPer were downloaded and saved as Maro-Enabled Workbook using Excel [81]. Then the *xy*-coordinates data from the CellTracker were copied onto the Maro-Enabled Workbook and further analysed using the corresponding Macros for the plot at origin, MSD curve, and directionality curve [81].

Staining of the actin filament Cells were treated with GO (s-GO and us-GO, 100 µg/mL, 0.5 mL/well, 24 h) or MβCD (5 mM, 0.5 mL/well, 4 h, C4555, Sigma), washed with pre-warmed PBS (0.5 mL/well, D8662, Sigma-Aldrich, Merck Sigma, UK), fixed with formaldehyde (3.7%, 0.5 ml/well, 10 min; 28908 Thermo Fisher Scientific, UK), permeabilized with Triton-X (0.1% in PBS (-/-), 0.5 mL/well, 10 min), re-washed with PBS (-/-) (0.5 mL/well, x 2, D8537, Sigma-Aldrich, Merck Sigma, UK), stained with Alexa Fluor™ 488 Phalloidin (1:1500 dilution prepared in PBS (-/-), 0.5 mL/well, 20 min, A12379, Thermo Fischer, UK). After staining, cells were washed with PBS (-/-) (0.5 mL/well, x 2) and ProLong™ Gold Antifade Mountant (P36930, Thermo Fisher Scientific, UK) was added to the cells. The cells were exposed to a higher concentration of GO (100 µg/mL) because the potential role of GO as an actin filament disrupting agent was investigated. Following the working principle for pharmaceutical inhibitors, the highest tested non-toxic concentration of inhibitor was used [28].Cells were imaged using Zeiss 780 CLSM with the 40X objective. Images were processed using Zeiss microscope software ZEN. Excitation/emission wavelength: Phalloidin = 495/518.

Flow cytometry

Cellular interactions with GO Cells were treated with s-GO or us-GO (50 µg/mL, 1 mL/well, 24 h). After treatment, cells were collected with and without washing. The cells without washing were detached with 0.05% Trypsin-EDTA (300 uL/well, 10 min), neutralised with FBS (30 uL/well), collected in 1.5 mL Eppendorf tube, and stored in ice until analysis. The cells with washing were washed with PBS (-/-) (1 mL/well, x 2), detached with 0.05% Trypsin-EDTA (300 uL/well, 10 min), neutralised with FBS (30 uL/well), collected in 1.5 mL Eppendorf tube, re-washed by centrifugation (500 RPM, 5 min, 4 ^{O}C, x 2), re-suspended in PBS (-/-) (300 uL/tube), and stored in ice until analysis. The samples were analysed by FACSVerse flow cytometry using PE-Cy7-A channel (band pass: 488 780/60). Excitation/emission band pass: GO = 594/620–690.

Cellular interactions with beads Cells were treated with the positively charged (+ 1 µm and + 0.2 µm) or negatively charged (–1 µm, –0.5 µm and –0.1 µm) beads (1.5 µL/mL, 1 mL/well, 24 h, F8765, F8764, F8823, F8813, F8803, Thermo Scientific, UK, respectively). After treatment, cells were detached with 0.05% Trypsin-EDTA (300 uL/well, 10 min), neutralised with FBS (30 uL/well), collected in 1.5 mL Eppendorf tube, stored in ice, and analysed by FACSVerse flow cytometry (bandpass: 488 530/30) using the FITC channel. Excitation/emission band pass: +1, + 0.2, -1, -0.5, -0.1 µm beads = 505/515.

Cellular interactions with graphene flakes Cells treated with Gr-TMA_3 or Gr-PS1(50 µg/mL, 1 mL/well, 24 h). After treatment, supernatants were removed, cells were detached with 0.05% Trypsin-EDTA (300 uL/well, 10 min), neutralised with FBS (30 uL/well), collected in 1.5 mL Eppendorf tube, stored in ice, and analysed by FACSVerse flow cytometry. A total population of 10 000 cells was acquired, and the mean side-scattering value was used for quantification of graphene flakes-cellular interaction. The data were statistically analyzed using GraphPad Prism (version 10.4.1).

TEM

Cells were seeded on sterilised Aclar placed in 24-well plate. Subsequently, cells were treated with s-GO or us-GO (50 µg/mL, 0.5 mL/well, 24 h) and fixed at room temperature (4% formaldehyde, 2.5% glutaraldehyde in 0.1 M HEPS budder, 0.5 mL/well, 1 h). Samples were postfixed with 1% osmium tetroxide + 1.5% potassium ferrocynaide in 0.1 M cacodylate buffer (pH 7.2) for 1 h, then in 1% uranyl acetate in water overnight. Then they

were dehydrated in ethanol series infiltrated with TAAB LV resin and polymerised for 24 h at 60 C degree. Sections were cut with Reichert Ultracut ultramicrotome and observed with FEI Tecnai 12 Biotwin microscope at 100 kV accelerating voltage. Images were taken with Gatan Orius SC1000 CCD camera.

Statistical analysis

Flow cytometry, cell speed, and directionality data were statistically analysed using GraphPad Prism (version 9 or 10). The analysis of variance (one-way or two-way with Tukey's multiple comparisons test was used for flow cytometry data (Figs. 4 and S20: one-way ANOVA, $n = 3$ with duplicates, Figs. 2e and S17: two-way ANOVA, $n = 3$ with duplicates, Figure S21: two-way ANOVA, $n = 1$ with duplicates). Cell speeds data were statistically analysed using unpaired T-test (Fig. 6) or analysis of variance (one-way ANOVA) with Dunn's multiple comparisons test and descriptive statistics (Fig. 7), and the result was reported as mean ± SD (number of cells analysed per condition ≥ 43). Directionality data were analysed using descriptive statistics, and the result was reported as mean ± SEM. *Statistically different: * $p < 0.05$, ** $p < 0.01$, *** $p < 0.001$ and **** $p < 0.0001$, ns = not significant.

Supplementary Information

The online version contains supplementary material available at https://doi.org/10.1186/s12951-025-03400-3.

Supplementary Material 1

Acknowledgements

We thank Dr Adrian Esteban Arranz for contributing to the synthesis of the specific GO batch used in the present study and Dr Miguel Arellano and Ms Angeliki Karakasidi for contributing to the characterization of the GO materials. The ICN2 is funded by the CERCA programme / Generalitat de Catalunya and has been supported by the Severo Ochoa Centres of Excellence programme [SEV-2017-0706] and is currently supported by the Severo Ochoa Centres of Excellence programme, Grant CEX2021-001214-S, both funded by MCIN/AEI/10.13039.501100011033. Y.C. acknowledge the studentship from the UK Research and Innovation (UKRI) Engineering and Physical Sciences Research Council (EPSRC) Centre for Doctoral Training programme (Graphene NOWNANO CDT; EP/L01548X/1). The authors acknowledge the Manchester Collaborative Centre for Inflammation Research (MCCIR) as the funding source for the FACSVerse.

Author contributions

SV conceived and supervised the work, and analysed results. YC and SV designed all the experiments. YC performed the experiments, analysed all the results, wrote the manuscript. VR, AM, DS performed flow cytometry, TEM analysis and confocal imaging analysis, respectively. NL, YS, CC provided the materials and characterisation used in this work. KK supervised preparation and characterisation of GO. Manuscript was written and edited by YC, SV and KK, with the input from NL.

Data availability

No datasets were generated or analysed during the current study.

Declarations

Ethics approval and consent to participate

Not applicable.

Consent for publication

Not applicable.

Competing interests

The authors declare no competing interests.

Received: 6 February 2025 / Accepted: 15 April 2025
Published online: 30 May 2025

References

1. Priyadarsini S, Mohanty S, Mukherjee S, Basu S, Mishra M. Graphene and graphene oxide as nanomaterials for medicine and biology application. J Nanostructure Chem. 2018;8:123–37.
2. Vincent M, De Lázaro I, Kostarelos K. Graphene materials as 2D non-viral gene transfer vector platforms. Gene Ther. 2017;24:123–32.
3. Rodrigues AF, Newman L, Lozano N, Mukherjee SP, Fadeel B, Bussy C, Kostarelos K. A blueprint for the synthesis and characterisation of thin graphene oxide with controlled lateral dimensions for biomedicine. 2D Mater. 2018;5:035020.
4. Chang Y, Yang S-T, Liu J-H, Dong E, Wang Y, Cao A, Liu Y, Wang H. In vitro toxicity evaluation of graphene oxide on A549 cells. Toxicol Lett. 2011;200:201–10.
5. Wu C, Wang C, Han T, Zhou X, Guo S, Zhang J. Insight into the cellular internalization and cytotoxicity of graphene quantum Dots. Adv Healthc Mater. 2013;2:1613–9.
6. Fong YT, Chen C-H, Chen J-P. Intratumoral delivery of doxorubicin on Folate-Conjugated graphene oxide by In-Situ forming Thermo-Sensitive hydrogel for breast Cancer therapy. Nanomaterials. 2017;7:388.
7. Ma N, Liu J, He W, Li Z, Luan Y, Song Y, Garg S. Folic acid-grafted bovine serum albumin decorated graphene oxide: an efficient drug carrier for targeted cancer therapy. J Colloid Interface Sci. 2017;490:598–607.
8. Tripathi SK, Goyal R, Gupta KC, Kumar P. Functionalized graphene oxide mediated nucleic acid delivery. Carbon. 2013;51:224–35.
9. Jin M, Liu Z, Zhang W, Dong H, Zhou F, Yu J, Wang X, Guo Z. Mitochondrial-Targeted polyethylenimine functionalized graphene oxide nanocarrier and its Anti-Tumor effect on human lung carcinoma cells. NANO. 2015;10:1550121.
10. Zhou L, Jiang H, Wei S, Ge X, Zhou J, Shen J. High-efficiency loading of hypocrellin B on graphene oxide for photodynamic therapy. Carbon. 2012;50:5594–604.
11. Lu C-H, Zhu CL, Li J, Liu JJ, Chen X, Yang HH. Using graphene to protect DNA from cleavage during cellular delivery. Chem Commun. 2010;46:3116–8.
12. Liu Z, Robinson JT, Sun X, Dai H. PEGylated nanographene oxide for delivery of water-insoluble cancer drugs-sup. J Am Chem Soc. 2008;130:10876–7.
13. Yu Q, Zhang B, Li J, Li M. The design of peptide-grafted graphene oxide targeting the actin cytoskeleton for efficient cancer therapy. Chem Commun. 2017;53:11433–6.
14. Wang Y, Sun G, Gong Y, Zhang Y, Liang X, Yang L. Functionalized Folate-Modified graphene Oxide/PEI SiRNA nanocomplexes for targeted ovarian Cancer gene therapy. Nanoscale Res Lett. 2020;15:1–11.
15. Robinson JT, Tabakman SM, Liang Y, Wang H, Casalongue HS, Vinh D, Dai H. Ultrasmall reduced graphene oxide with high near-infrared absorbance for photothermal therapy. J Am Chem Soc. 2011;133:6825–31.
16. Jin C, Wang F, Tang Y, Zhang X, Wang J, Yang Y. Distribution of graphene oxide and TiO_2-Graphene oxide composite in A549 cells. Biol Trace Elem Res. 2014;159:393–8.
17. Sun X, Liu Z, Welsher K, Robinson JT, Goodwin A, Zaric S, Dai H. Nano-graphene oxide for cellular imaging and drug delivery. Nano Res. 2008;1:203–12.
18. Quagliarini E, Santo RD, Pozzi D, Tentori P, Cardarelli F, Caracciolo G. Mechanistic insights into the release of doxorubicin from graphene oxide in cancer cells. Nanomaterials. 2020;10:1–11.
19. Buskaran K, Hussein MZ, Moklas MAM, Fakurazi S. Morphological changes and cellular uptake of functionalized graphene oxide loaded with Protocatechuic acid and folic acid in hepatocellular carcinoma cancer cell. Int J Mol Sci. 2020;21:1–16.

20. Tian X, Yang Z, Duan G, Wu A, Gu Z, Zhang L, Chen C, Chai Z, Ge C, Zhou R. Graphene oxide nanosheets retard cellular migration via disruption of actin cytoskeleton. Small. 2017;13:1–10.
21. Duan G, Kang S, Tian X, Garate JA, Zhao L, Ge C, Zhou R. Protein Corona mitigates the cytotoxicity of graphene oxide by reducing its physical interaction with cell membrane. Nanoscale. 2015;7:15214–24.
22. Lammel T, Boisseaux P, Fernández-Cruz M-L, Navas JM. Internalization and cytotoxicity of graphene oxide and carboxyl graphene nanoplatelets in the human hepatocellular carcinoma cell line hep G2. Part Fibre Toxicol. 2013;10:1–21.
23. Zhang H, Peng C, Yang J, Lv M, Liu R, He D, Fan C, Huang Q. Uniform ultrasmall graphene oxide nanosheets with low cytotoxicity and high cellular uptake. ACS Appl Mater Interfaces. 2013;5:1761–7.
24. Zhu J, Li B, Xu M, Liu R, Xia T, Zhang Z, Xu Y, Liu S. Graphene oxide promotes Cancer metastasis through associating with plasma membrane to promote TGF-β Signaling-Dependent Epithelial-Mesenchymal transition. ACS Nano. 2020;14:818–27.
25. Huang J, Zong C, Shen H, Liu M, Chen B, Ren B, Zhang Z. Mechanism of cellular uptake of graphene oxide studied by Surface-Enhanced Raman spectroscopy. Small. 2012;8:2577–84.
26. Qin XC, Guo ZY, Liu ZM, Zhang W, Wan MM, Yang BW. Folic acid-conjugated graphene oxide for cancer targeted chemo-photothermal therapy. J Photochem Photobiol B Biol. 2013;120:156–62.
27. Heo J, Tanum J, Park S, Choi D, Jeong H, Han U, Hong J. Controlling physicochemical properties of graphene oxide for efficient cellular delivery. J Ind Eng Chem. 2020;88:312–8.
28. Vranic S, Rodrigues AF, Buggio M, Newman L, White MRH, Spiller DG, Bussy C, Kostarelos K. Live imaging of Label-Free graphene oxide reveals critical factors causing oxidative Stress-Mediated cellular responses. ACS Nano. 2018;12:1373–89.
29. de Lázaro I, Vranic S, Marson D, Rodrigues AF, Buggio M, Esteban-Arranz A, Mazza M, Posocco P, Kostarelos K. Graphene oxide as a 2D platform for complexation and intracellular delivery of SiRNA. Nanoscale. 2019;11:13863–77.
30. Shin Y, Vranic S, Just-Baringo X, Gali SM, Kisby T, Chen Y, Gkoutzidou A, Prestat E, Belijonne D, Larrosa I, Kostarelos K, Casiraghi C. Stable, concentrated, biocompatible, and defect-free graphene dispersions with positive charge. Nanoscale. 2020;12:12383–94.
31. Kucki M, Diener L, Bohmer N, Hirsch C, Frug HF, Palermo V, Wick P. Uptake of label-free graphene oxide by Caco-2 cells is dependent on the cell differentiation status. J Nanobiotechnol. 2017;15:1–18.
32. Mu Q, Su G, Li L, Gilbertson BO, Yu LH, Zhang Q, Sun Y-P, Yan B. Size-Dependent cell uptake of Protein-Coated graphene oxide nanosheets. ACS Appl Mater Interfaces. 2012;4:2259–66.
33. Babadaei MMN, Moghaddam MF, Solhvand S, Alizadehmollayaghoob E, Attar F, Rajabbeigi E, Akhtari K, Sari S, Falahati M. Biophysical, bioinformatical, cellular, and molecular investigations on the effects of graphene oxide nanosheets on the hemoglobin structure and lymphocyte cell cytotoxicity. Int J Nanomed. 2018;13:6871–84.
34. Mendes RG, Mandarino A, Koch B, Meyer AK, Bachmatiuk A, Hirsch C, Gemming T, Schmidt OG, Liu Z, Rümmeli MH. Size and time dependent internalization of label-free nano-graphene oxide in human macrophages. Nano Res. 2017;10:1980–95.
35. Wang B, Su X, Liang J, Yang L, Hu Q, Shan X, Wan J, Hu Z. Synthesis of polymer-functionalized nanoscale graphene oxide with different surface charge and its cellular uptake, biosafety and immune responses in Raw264.7 macrophages. Mater Sci Eng C. 2018;90:514–22.
36. Seemork J, Sansureerungsikul T, Sathornsantikun K, Sinthusake T, Shigyou K, Tree-Udom T, Jiangchareon B, Chiablaem K, Lirdrapamongkol K, Svasti J, Hamada T, Palaga T, Wanichwecharunggruang S. Penetration of oxidized carbon nanospheres through lipid bilayer membrane: comparison to graphene oxide and oxidized carbon nanotubes, and effects of pH and membrane composition. ACS Appl Mater Interfaces. 2016;8:23549–57.
37. Tian J, Ding L, Wang Q, Hu Y, Jia L, Yu J-S, Ju H. Folate Receptor-Targeted and cathepsin B-Activatable nanoprobe for in situ therapeutic monitoring of photosensitive cell death. Anal Chem. 2015;87:3841–8.
38. Li J, Wang X, Mei K-C, Chang CH, Jiang J, Liu X, Liu Q, Guiney LM, Hersam MC, Liao Y-P, Meng H, Xia T. Lateral size of graphene oxide determines differential cellular uptake and cell death pathways in Kupffer cells, LSECs, and hepatocytes. Nano Today. 2021;37:1–18.
39. Mauro N, Scialabba C, Agnello S, Cavallaro G, Giammona G. Folic acid-functionalized graphene oxide nanosheets via plasma etching as a platform to combine NIR anticancer phototherapy and targeted drug delivery. Mater Sci Eng C. 2020;107:1–9.
40. Mendes RG, Koch B, Bachmatiuk A, Ma X, Sanchez S, Damm C, Schmidt OG, Gemming T, Eckert J, Rmmeli MH. A size dependent evaluation of the cytotoxicity and uptake of nanographene oxide. J Mater Chem B. 2015;3:2522–9.
41. Zhu J, Xu M, Gao M, Zhang Z, Xu Y, Xia T, Liu S. Graphene oxide induced perturbation to plasma membrane and cytoskeletal meshwork sensitize Cancer cells to chemotherapeutic agents. ACS Nano. 2017;11:2637–51.
42. Matesanz M-C, Vila M, Feito M-J, Linares J, Gonçalves G, Vallet-Regi M, Marques P-AAP, Portolés M-T. The effects of graphene oxide nanosheets localized on F-actin filaments on cell-cycle alterations. Biomaterials. 2013;34:1562–9.
43. Linares J, Matesanz MC, Vila M, Feito MJ, Goncalves G, Vallet-Regi M, Marques PAAP, Portoles MT. Endocytic mechanisms of graphene oxide nanosheets in osteoblasts, hepatocytes and macrophages. ACS Appl Mater Interfaces. 2014;6:13697–706.
44. Martinez Paino IM, Santos F, Zucolotto V. Biocompatibility and toxicology effects of graphene oxide in cancer, normal, and primary immune cells. J Biomed Mater Res Part A. 2017;105A:728–36.
45. Yue H, Wei W, Yue Z, Wang B, Luo N, Gao Y, Ma D, Ma G, Su Z. The role of the lateral dimension of graphene oxide in the regulation of cellular responses. Biomaterials. 2012;33:4013–21.
46. Vila M, Portols MT, Marques PAAP, Feito MJ, Matesanz MC, Ramrez-Santilln C, Gonçalves G, Cruz SMA, Nieto A. Vallet-Regi, Cell uptake survey of pegylated nanographene oxide. Nanotechnology. 2012;23:465103.
47. Chen Y, Rivers-Auty J, Cric LE, Barr K, Rosano V, Arranz AE, Loret T, Spiller D, Bussy C, Kostarelos K, Vranic S. Dynamic interactions and intracellular fate of label-free, thin graphene oxide sheets within mammalian cells: Role of lateral sheet size. Nanoscale Adv. 2021;3:4166–85.
48. de Lázaro I, Sharp P, Gurcan C, Ceylan A, Stylianou M, Kisby T, Chen Y, Vranic S, Barr K, Taheri H, Ozen A, Bussy C, Yilmazer A, Kostarelos K. Deep tissue translocation of graphene oxide sheets in human glioblastoma 3D spheroids and an orthotopic xenograft model. Adv Ther. 2021;4:1–15.
49. Hou JC-H, Gandhi JG, Zia RN, Paszek MJ. Physical biology of the cancer cell glycocalyx. Nat Phys. 2018;14:658–69.
50. Alves AC, Ribeiro D, Nunes C, Reis S. Biophysics in cancer: the relevance of drug-membrane interaction studies. Biochim Biophys Acta. 2016;1858:2231–44.
51. Yang H, Hernandez Y, Schlierf A, Felten A, Eckmann A, Johal S, Louette P, Pireaux J-J, Feng X, Müellen K, Palermo V, Casiraghi C. A simple method for graphene production based on exfoliation of graphite in water using 1-pyrenesulfonic acid sodium salt. Carbon. 2013;53:357–65.
52. Chen Y, Taufiq T, Zeng N, Lozano N, Karakasidi A, Church H, Jovanovic A, Jones SA, Panigrahi A, Larrosa I, Kostarelos K, Casiraghi C, Vranic S. Defect-free graphene enhances enzyme delivery to fibroblasts derived from the patients with lysosomal disorders. Nanoscale. 2023;15:9348–64.
53. Zhang C, Yan L, Wang X, Zhu S, Chen C, Gu Z, Zhao Y. Progress, challenges, and future of nanomedicine. Nano Today. 2020;35:101008.
54. Nel AE, Mädler L, Velegol D, Xia T, Hoek EMV, Somasundaran P, Klaessig F, Castranova V, Thompson M. Understanding biophysicochemical interactions at the nano-bio interface. Nat Mater. 2009;8:543–57.
55. Oh N, Park J-H. Endocytosis and exocytosis of nanoparticles in mammalian cells. Int J Nanomed. 2014;9:51–63.
56. Wang J, Wei Y, Shi X, Gao H. Cellular entry of graphene nanosheets: the role of thickness, oxidation and surface adsorption. RSC Adv. 2013;3:15776–82.
57. Guo Z, Chakraborty S, Monikh FA, Varsou D-D, Chetwynd AJ, Afantitis A, Lynch I, Zhang P. Surface functionalization of Graphene-Based materials: biological behavior, toxicology, and Safe-By-Design aspects. Adv Biology. 2021;5:2100637.
58. Mukherjee SP, Lazzaretto B, Hultenby K, Newman L, Rodrigues AF, Lozano N, Kostarelos K, Malmberg P, Fadeel B. Graphene oxide elicits membrane lipid changes and neutrophil extracellular trap formation. Chem. 2018;4:334–58.
59. Bramini M, Chiacchiaretta M, Armirotti A, Rocchi A, Kale DD, Martin C, Vzquez E, Bandiera T, Ferroni S, Cesca F, Benfenati F. An Increase in Membrane Cholesterol by Graphene Oxide Disrupts Calcium Homeostasis in Primary Astrocytes. Small. 2019;15:1900147.
60. Zhou H, Zhang B, Zheng J, Yu M, Zhou T, Zhao K, Jia Y, Gao X, Chen C, Wei T. The Inhibition of migration and invasion of cancer cells by graphene via the impairment of mitochondrial respiration. Biomaterials. 2014;35:1597–607.
61. Kadzik RS, Homa KE, Kovar DR. Cytoskeleton network Self-Organization through competition and Cooperation. Annu Rev Cell Dev Biol. 2020;36:35–60.

62. Blanchoin L, Boujemaa-Paterski R, Sykes C, Plastino J. Actin dynamics, architecture, and mechanics in cell motility. Physiol Rev. 2014;94:235–63.
63. Kashani AS, Packirisamy M. Cancer-Nano-Interaction: from cellular uptake to Mechanobiological responses. Int J Mol Sci. 2021;22:9587.
64. Ivanov AI. Exocytosis and endocytosis. Totowa: Humana; 2008.
65. Bera S, Ghosh S, Ali A, Pal M, Chakrabarti P. Inhibition of microtubule assembly and cytotoxic effect of graphene oxide on human colorectal carcinoma cell HCT116. Arch Biochem Biophys. 2021;708:108940.
66. Rudzka DA, Spennati G, McGarry DJ, Chim Y-H, Neilson M, Ptak A, Munro J, Kalna G, Hedley A, Moralli D, Green C, Mason S, Blyth K, Mullin M, Yin H, Olson MF. Migration through physical constraints is enabled by MAPK-induced cell softening via actin cytoskeleton re-organization. J Cell Sci. 2019;132:jcs224071.
67. Huang C, Butler PJ, Tong S, Muddana HS, Bao G, Zhang S. Substrate stiffness regulates cellular uptake of nanoparticles. Nano Lett. 2013;13:1611–5.
68. Wei X, Wei R, Jiang G, Jia Y, Lou H, Yang Z, Luo D, Huang Q, Xu S, Yang X, Zhou Y, Li X, Ji T, Hu J, Xi L, Ma D, Ye F, Gao Q. Mechanical cues modulate cellular uptake of nanoparticles in cancer via clathrin-mediated and caveolae-mediated endocytosis pathways. Nanomed (Lond). 2019;14:613–26.
69. Wang Y, Gong T, Zhang Z-R, Fu Y. Matrix stiffness differentially regulates cellular uptake behavior of nanoparticles in two breast Cancer cell lines. ACS Appl Mater Interfaces. 2017;9:25915–28.
70. Kruger TM, Bell KJ, Lansakara TI, Tivanski AV, Doorn JA, Stevens LL. Reduced extracellular matrix stiffness prompts SH-SY5Y cell softening and actin turnover to selectively increase Aβ(1–42) endocytosis. ACS Chem Neurosci. 2019;10:1284–93.
71. Alibert C, Goud B, Manneville J-B. Are cancer cells really softer than normal cells? Biol Cell. 2017;109:167–89.
72. Ghorbani M, Soleymani H, Hashemzadeh H, Mortezazadeh S, Sedghi M, Shojaeilangari S, Allahverdi A, Naderi-Manesh H. Microfluidic investigation of the effect of graphene oxide on mechanical properties of cell and actin cytoskeleton networks: experimental and theoretical approaches. Sci Rep. 2021;11:16216.
73. Bezanilla M, Gladfelter AS, Kovar DR, Lee W-L. Cytoskeletal dynamics: A view from the membrane. J Cell Biol. 2015;209:329–37.
74. Kwik J, Boyle S, Fooksman D, Margolis L, Sheetz MP, Edidin M. Membrane cholesterol, lateral mobility, and the phosphatidylinositol 4,5-bisphosphate-dependent organization of cell actin. PNAS USA. 2003;100:13964–9.
75. Mollinedo F, Gajate C. Lipid rafts as signaling hubs in cancer cell survival/death and invasion: implications in tumor progression and therapy. J Lipid Res. 2020;61:611–35.
76. Dória ML, Cotrim Z, Macedo B, Simões C, Domingues P, Helguero L, Domingues MR. Lipidomic approach to identify patterns in phospholipid profiles and define class differences in mammary epithelial and breast cancer cells. Breast Cancer Res Treat. 2012;133:635–48.
77. Olson MF, Sahai E. The actin cytoskeleton in cancer cell motility. Clin Exp Metastasis. 2009;26:273–87.
78. Smythe E, Ayscough KR. Actin regulation in endocytosis. J Cell Sci. 2006;119:4589–98.
79. Wagner R, Rosenberg M, Estensen R. Endocytosis in Chang liver cells: quantitation by Sucrose-^{3}H uptake and Inhibition by cytochalasin B. J Cell Biol. 1971;50:804–17.
80. MacLean-Fletcher S, Pollard TD. Mechanism of action of cytochalasin B on actin. Cell. 1980;20:329–41.
81. Gorelik R, Gautreau A. Quantitative and unbiased analysis of directional persistence in cell migration. Nat Protoc. 2014;9:1931–43.
82. Loret T, Augusto Visani L, de Luna A, Fordham A, Arshad K, Barr N, Lozano K, Kostarelos, Bussy C. Innate but not adaptive immunity regulates lung recovery from chronic exposure to graphene oxide nanosheets. Adv Sci. 2022;2104559:1–16.
83. Piccinini F, Kiss A, Horvath P. CellTracker (not only) for dummies. Bioinformatics. 2016;32:955–7.

Publisher's note